Tunable Liquid Gradient Refractive Index (L-GRIN) lens with two degrees of freedom†

Xiaole Mao,[ab] Sz-Chin Steven Lin,[a] Michael Ian Lapsley,[a] Jinjie Shi,[a] Bala Krishna Juluri[a] and Tony Jun Huang*[ab]

Received 19th December 2008, Accepted 25th March 2009
First published as an Advance Article on the web 15th April 2009
DOI: 10.1039/b822982a

We report a tunable optofluidic microlens configuration named the Liquid Gradient Refractive Index (L-GRIN) lens for focusing light within a microfluidic device. The focusing of light was achieved through the gradient refractive index (GRIN) within the liquid medium, rather than *via* curved refractive lens surfaces. The diffusion of solute ($CaCl_2$) between side-by-side co-injected microfluidic laminar flows was utilized to establish a hyperbolic secant (HS) refractive index profile to focus light. Tailoring the refractive index profile by adjusting the flow conditions enables not only tuning of the focal distance (translation mode), but also shifting of the output light direction (swing mode), a second degree of freedom that to our knowledge has yet to be accomplished for in-plane tunable microlenses. Advantages of the L-GRIN lens also include a low fluid consumption rate, competitive focusing performance, and high compatibility with existing microfluidic devices. This work provides a new strategy for developing integrative tunable microlenses for a variety of lab-on-a-chip applications.

Introduction

Tunable microlenses have proven to be crucial components for incorporating advanced functionalities into microfluidic or lab-on-a-chip systems.[1] A tunable microlens adaptively reshapes the input light, adjusting its focal position, intensity, beam profile, and even propagation direction. Such fine tuning of the light is critical for realizing a broad spectrum of lab-on-a-chip applications such as flow cytometry,[2,3] single molecule detection,[4] and on-chip optical tweezers.[5–7]

Nearly all tunable microlenses developed so far are classic refractive lenses and their working mechanism is straightforward: light beams bend when impinging upon the curved refractive lens surfaces and are subsequently brought to focus; the change of curvatures of refractive surfaces results in the change of focal distances. Many out-of-plane tunable microlenses, which focus light in the direction perpendicular to the microfluidic device plane, have been successfully developed from this concept. These tunable microlenses provide adaptive focusing with adjustable curved refractive surfaces, such as micro meniscus surface actuated by electrowetting[8] and stimuli-responsive hydrogels,[9] and hydraulically actuated polydimethylsiloxane (PDMS) membranes.[10,11] From device integration perspective, however, in-plane tunable microlenses which focus light parallel to the device plane are more preferable as they can be simultaneously fabricated and seamlessly integrated with other on-chip fluidic and optical components such as on-chip lasers[12–14] and waveguides,[15,16] thus avoiding the complications in optical alignment and device integration often occurring in out-of-plane microlenses. On the other hand, due to the limitation of planar device structures, it is difficult to readily adapt the lens tuning mechanism of out-of-plane microlens to in-plane ones. As a result, the majority of in-plane microlenses demonstrated thus far were built with the non-tunable solid (*e.g.*, PDMS) curved refractive surfaces with fixed focal length.[2,3,17,18]

The challenges of implementing adjustable refractive microlens surfaces within the microfluidic device plane were recently addressed with a group of tunable in-plane optofluidic microlenses. Optofluidic technology[19,20] exploits the unique properties of microfluidic flows to manipulate the light in microscale. The refraction of light at curved, optically-smooth, liquid–liquid interfaces between co-injected microfluidic laminar flows with different refractive indices were utilized to realize the tunable microlenses within the microfluidic device plane. Previously, we reported a tunable optofluidic cylindrical microlens[21] by "bending" a $CaCl_2/H_2O$ liquid–liquid interface using the Dean Flow effect.[22–24] More recently, the Whitesides group introduced a dynamically reconfigurable liquid–liquid lens[25] which exploited the convex shape of liquid–liquid interfaces in a microfluidic expansion chamber. In both cases, curvatures of the liquid–liquid interfaces were hydrodynamically modulated by simply adjusting the flow conditions, and excellent flexibilities for lens tuning have been achieved. The drawback of such methods, however, lies in the fact that in order to avoid the smearing of the lens surfaces (liquid–liquid interfaces) caused by diffusive mixing, a relatively high flow velocity is needed to minimize the residence time of the fluids in focusing region. Therefore, the fluid consumption rates of such lenses are relatively high (hundreds of $\mu l\ m^{-1}$). Such high flow rates have created difficulties in sustaining the lens over a prolonged period. They also impose unrealistic requirement for developing integrative on-chip pumps[26] for lens control.

[a]*Department of Engineering Science and Mechanics, The Pennsylvania State University, University Park, PA, 16802, USA. E-mail: junhuang@psu.edu; Fax: +1 814-865-9974; Tel: +1 814-863-4209*
[b]*Department of Bioengineering, The Pennsylvania State University, University Park, PA, 16802, USA*

† Electronic supplementary information (ESI) available: Fabrication details and additional experimental results; Video S1 for Fig. 3 and Video S2 for Fig. 6. See DOI: 10.1039/b822982a

The above-mentioned difficulties in creating and sustaining an in-plane tunable classic refractive microlens challenge us to search for alternative solutions. In this work, we report an in-plane tunable microlens configuration that does not require a curved lens surface. The method was named the Liquid Gradient Refractive Index (L-GRIN) lens, as its focusing mechanism resembles that of the solid-based Gradient Refractive Index (GRIN) lens which is widely used in the optical fiber industry for coupling and collimation.[27] A GRIN lens often has a transversely (perpendicular to the optical axis) variable refractive index and a flat lens structure, in contrast to the curved lens surface of a classic refractive lens. Rather than abruptly changing its direction at the surfaces of classic refractive lenses (Fig. 1A1), light travelling along the optical axis within such a GRIN lens is gradually bent toward the optical axis and brought to a focusing point (Fig. 1A2). The key to realizing a GRIN lens is to establish light-focusing refractive index gradient profiles within the lens material. Establishment of such refractive index gradient profiles in solid materials (*e.g.*, glass) is difficult and often involves complex fabrication processes such as microcontrolled dipcoating, field-assisted ion-exchange, or vapor deposition,[28] and the focusing cannot be tuned due to the fixed refractive index gradient.

We have recognized that in microfluidic systems, refractive index gradients can be readily obtained through controlled diffusion of solutes[29] or heat.[30] From this observation we propose a liquid-based GRIN lens that can conveniently adjust its refractive index gradient, and hence the focusing pattern, by manipulating the progress of diffusion. In the proposed L-GRIN lenses, diffusion favors, rather than hinders, the working mechanism of the tunable microlens. Therefore, the L-GRIN lens can operate at much-reduced flow rates, and the fluid consumption can be dramatically lowered from the existing in-plane tunable liquid–liquid microlenses.[21,25] More importantly, with precise microfluidic manipulation, one can change not only the focal distance of the L-GRIN lens (Fig. 1A2 to 1A3) by adjusting the refractive index contrast (difference between the maximum and minimum in the gradient), but also the direction of output light (Fig. 1A3 to 1A4) by shifting the optical axis. Such a tunable microlens with two degrees of freedom enables an unprecedented flexibility for on-chip manipulation of light.

Materials and methods

A variety of refractive index gradient profiles, such as parabolic[27,31] and hyperbolic secant (HS) profiles,[28,32,33] have been studied for their light-focusing properties. In the proposed L-GRIN lens, the establishment of light-focusing refractive index gradient solely relies on the diffusion of the solute within the fluidic flows. Therefore in this study we chose the HS profile because its mathematical resemblance to the error function (analytical solution to linear diffusion problem)[34] suggests that one may establish such a gradient through the diffusion in

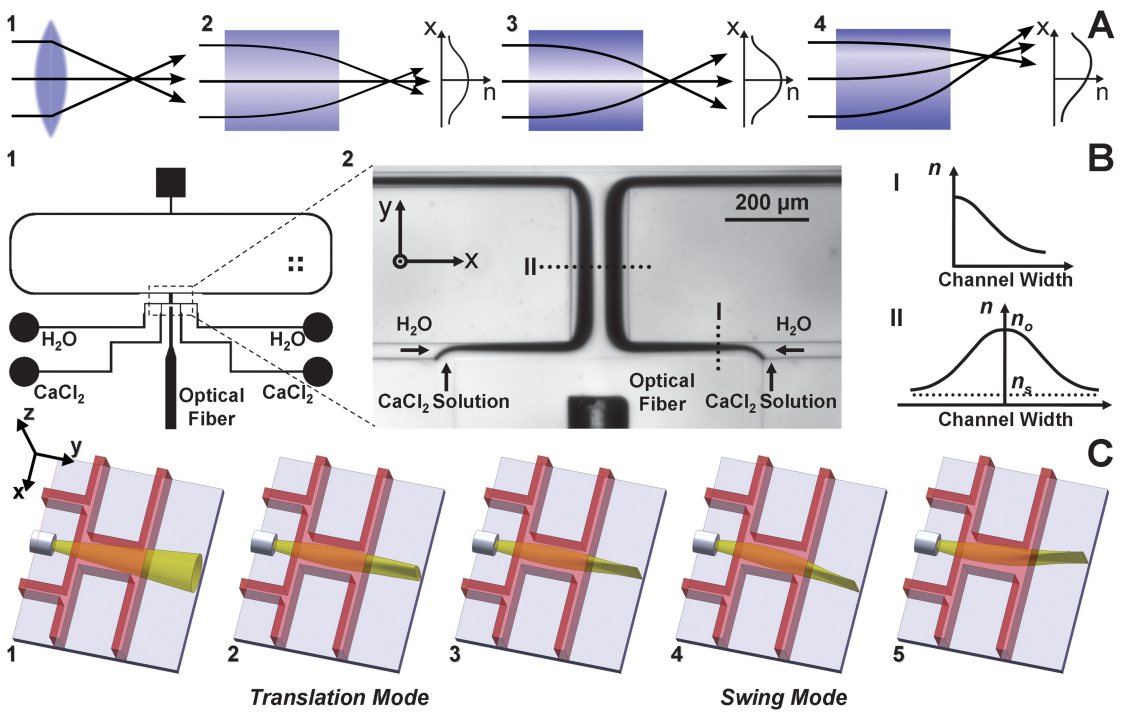

Fig. 1 Principle and design of the L-GRIN lens. (A) A schematic diagram showing the comparison between the classic refractive lens (A1) and GRIN lens (A2). Change of the refractive index contrast in GRIN lens can result in change of focal distance (A2–A3), and shift of optical axis can result in change of output light direction (A4). (B) Schematic of the L-GRIN lens design (B1), microscopic image of the L-GRIN lens in operation (B2, left), and the expected refractive index distribution at two locations (I and II) inside the lens (B2, right). High optical contrast areas (dark streaks) were observed near the fluidic boundaries (B2, left), suggesting significant variation of refractive index due to the $CaCl_2$ diffusion. (C) Schematic drawing showing two operation modes of the L-GRIN lens: the translation mode with variable focal length including no-focusing (C1), a large focal distance (C2), and a small focal distance (C3); and the swing mode with variable output light direction (C3–C5).

a side-by-side laminar flow configuration. The refractive index distribution of the HS profile is given by[28]

$$n^2(x) = n_s^2 + (n_0^2 - n_s^2)\mathrm{sech}^2(\alpha x) \quad (1)$$

where $n(x)$ is the refractive index of the GRIN material at any given transverse position x, n_0 is the highest refractive index at the center axis of the material, n_s is the background (lowest) refractive index of the material, and α is the gradient parameter. With the HS refractive index profile, the input light beams can be bent smoothly toward the optical axis of the GRIN material and brought to a focusing point. The trajectory of light within the material is determined by the refractive index distribution and can be analytically solved.

The schematic of the L-GRIN lens design is shown in Fig. 1B1. The device included four inlets and two outlet branches (two branches share a common outlet in order to maintain the equal back-pressure at both sides). $CaCl_2$ solution (3.5 M, $n_D \sim 1.41$) and H_2O ($n_D \sim 1.33$) were injected into the device as shown in Fig. 1B1. The refractive index of the mixture is linearly dependent on the $CaCl_2$ concentration. Fig. 1B2 depicts a typical flow pattern in the L-GRIN device with $CaCl_2$ flow rates and H_2O flow rates at both sides being 3.0 μl m^{-1} and 1.8 μl m^{-1}, respectively. On each side, two fluids of different refractive indices merged to form co-injected laminar flows and establish a $CaCl_2$ concentration distribution that resembles the error function or half of the HS profile (cross-section I, Fig. 1B2). The convergence of co-injected streams from both sides eventually results in a complete HS-like refractive index distribution (cross-section II, Fig. 1B2) in the main channel. The refractive index profile within the main channel can be readily adjusted by changing the flow rate from different inlets.

The input light from a semiconductor laser diode (wavelength = 532 nm) or a halogen white-light source (Ocean Optics) was coupled into the L-GRIN lens using a multi-mode optical fiber (Ocean Optics, outer diameter = 155 μm, core diameter = 50 μm, and nominal numerical aperture NA = 0.22). The optical fiber was aligned with the L-GRIN lens through a guide channel. The thickness of PDMS between the aperture of the optical fiber and the microfluidic channel was 100 μm. The height of channels was 155 μm throughout the device. The L-GRIN main channel has a width of 160 μm. Two designs were used for different experimental characterizations. They only differ in the length of the main channel, including a "long version" (main channel length = 400 μm, shown in Fig. 1B) and a "short version" (main channel length = 250 μm). All fluidic inlet and outlet channels were 50 μm wide. The L-GRIN device was fabricated using standard soft lithography. The injection of fluids was carried out using precision syringe pumps (KD Scientific 210). The image acquisition was performed using an inverted optical microscope (Nikon TE 2000U), a 16-bit monochromatic CCD camera (CoolSNAP HQ2), and a color digital camera (Nikon).

Fig. 1C depicts the two operation modes of the L-GRIN lens, namely the "translation mode" and the "swing mode." In both modes, the flow rates of $CaCl_2$ solutions remained unchanged. In the translation mode, the refractive index contrast (difference between n_0 and n_s in Eq. 1) can be adjusted by symmetrically changing the flow rates of H_2O from both sides to realize different focal lengths, such as no focusing (Fig. 1C1), a large focal length (Fig. 1C2), and a short focal length (Fig. 1C3). In the swing mode, the direction of the output light can be adjusted in device plane by shifting the optical axis of the L-GRIN lens with asymmetrical adjustment of H_2O flow rates from each side (Fig. 1C3 to 1C5). One can operate two modes independently or in combination.

To simulate and thus optimize the refractive index distribution and light propagation in the L-GRIN lens at different flow conditions, we adapted a combined approach of computational fluid dynamics (CFD) and optical ray-tracing simulation. The CFD simulation was conducted using a finite-volume based commercial package, CFD-ACE + (ESI-CFD, U.S.A). A user-routine code was developed to couple the viscosity and density of the solution with variable $CaCl_2$ concentrations in the CFD simulation.[21] Grid density-independence tests were performed to ensure that the grid density was sufficient. Refractive index distribution obtained from CFD simulations was used for the optical ray-tracing to study the trajectories of light during the focusing process. The ABCD law based ray-tracing algorithm for HS refractive index gradient[29] was written in MATLAB®. More details of device fabrication and experiment setup can be found in the ESI (Figs. S1 and S2).†

Result and discussions

Translation mode

In the translation mode, the fluidic injection rates were symmetric about the axis of the device. The $CaCl_2$ solution flow rates were kept constant and H_2O flow rates were adjusted to change the refractive index contrast within the main channel. The translation mode was studied using a long-version L-GRIN lens (main channel length = 400 μm) in order to cover a larger focal length range. We first performed CFD studies on the distribution of the $CaCl_2$ concentration[21] in the L-GRIN lens at different flow conditions. The $CaCl_2$ concentration distribution for a representative flow condition ($CaCl_2$ flow rates = 3.0 μl m^{-1}, H_2O flow rates = 1.8 μl m^{-1}) is shown in Fig. 2A, which matches well with the experimental result shown in Fig. 1B2. Fig. 2B shows cross-sectional refractive index profiles at five different locations (cross-sections 1–5, as indicated in Fig. 2A). The results indicate that the $CaCl_2$ concentration/refractive index profile were stable along the length of the L-GRIN lens (cross-sections 2–4). At the two ends of the L-GRIN lens (cross-sections 1 and 5), however, the refractive index was almost uniform across the channel width, with a value close to that of the PDMS (~1.41). The matched refractive indices between the fluids and PDMS reduced the light scattering lost caused by the rough surfaces of PDMS channels.[25] Changing the flow conditions ($CaCl_2$ flow rates = 3.0 μl m^{-1}, H_2O flow rates = 0.6, 1.2, 1.8, 2.4, and 3.0 μl m^{-1}, respectively) yielded different refractive index profiles in the L-GRIN lens (cross-section 3), as shown in Fig. 2C. The figure shows that with the fixed $CaCl_2$ flow rate, higher H_2O flow rates result in larger refractive index contrast. We also noticed that the simulated refractive index distributions in the L-GRIN lens can be well fitted with the HS curves described in Eq. 1.

The parameters extracted from the CFD simulation were used to conduct ray-tracing simulations for predicting the trajectories of the input light during the focusing process (Fig. 2D). The

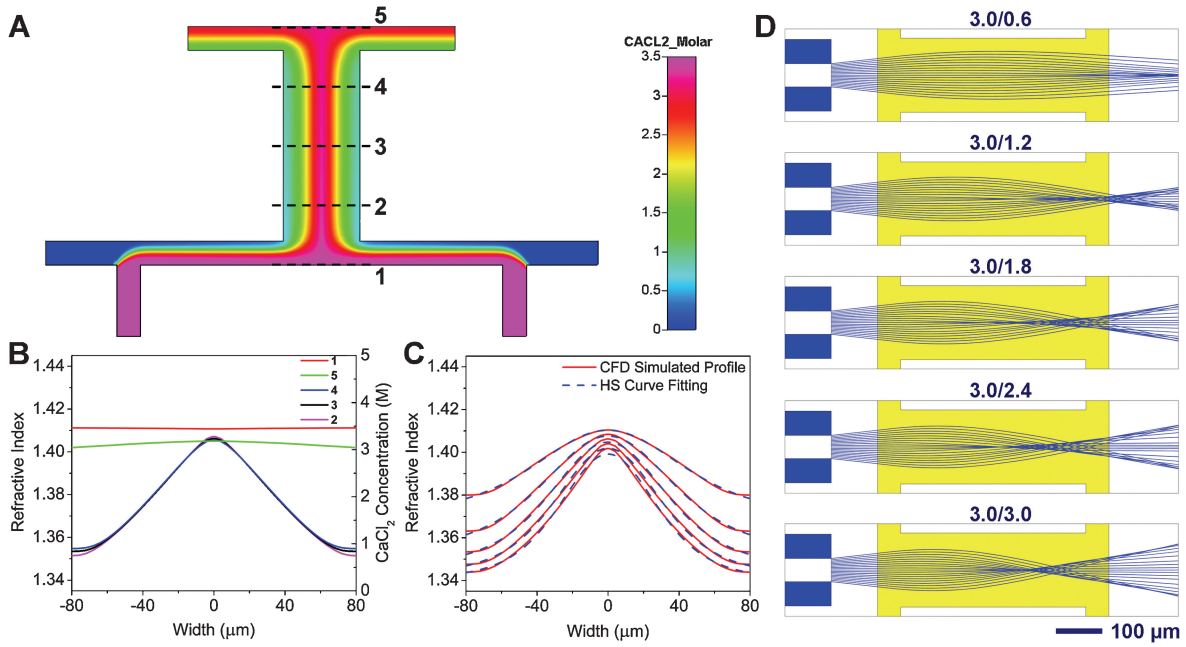

Fig. 2 CFD and ray tracing simulation for the translation mode. (A) Simulated $CaCl_2$ concentration distribution in a long-version L-GRIN lens ($CaCl_2$ flow rate = 3.0 μl m^{-1} and H_2O flow rate = 1.8 μl m^{-1}). The color bar represents the molar concentration of $CaCl_2$. (B) Cross-sectional $CaCl_2$ concentration/refractive index profiles at different locations (top to bottom: cross-sections 1, 5, 4, 3, and 2, respectively, as defined in Fig. 2A). (C) Refractive index profile at the middle of the L-GRIN lens (cross-section 3 defined in Fig. 2A) for different flow conditions (top to bottom, the $CaCl_2$ flow rates were fixed at 3.0 μl m^{-1}, and the H_2O flow rates were 0.6, 1.2, 1.8, 2.4, and 3.0 μl m^{-1}, respectively). Dotted lines are HS curve fitting. (D) Ray-tracing simulation in a long-version L-GRIN lens using the parameters obtained from the CFD simulation. The flow conditions are indicated in the graph (*e.g.*, 3.0/3.0 represents $CaCl_2$ flow rates = 3.0 μl m^{-1}, and H_2O flow rates = 3.0 μl m^{-1}, respectively).

trajectories of the light beams were analytically solved using the ABCD law[29] between cross-sections 2 and 4. In the transition regions where the ABCD law was not applicable due to the variable refractive index along the channel length, the refractive index domain was discretized and the beam was traced grid-to-grid using the Snell's law.[21] The ray-tracing simulations clearly show that the focal length can be adjusted by changing flow conditions. Higher H_2O flow rates (when $CaCl_2$ flow rates are constant) result in larger refractive index contrast, which causes light to bend toward the lens axis more significantly and leads to the decreased focal distance.

The ray-tracing experiments for the translation mode are shown in Fig. 3. To observe the trajectory of the input light beam (from a semiconductor laser diode, wavelength = 532 nm) in the L-GRIN lens during the variable focusing process, we dyed both $CaCl_2$ solution and H_2O with fluorescent dye rhodamine B (10 μg ml^{-1}; excitation wavelength = 532 nm; emission wavelength = 560 nm). With rhodamine-dyed solution, the light path within the L-GRIN lens shows a reddish color due to the fluorescent emission of the rhodamine. Light passing through the PDMS substrate near the channel wall displays a green or yellowish color, which can be attributed to the scattered laser excitation light (green), or combined effects of the scattered laser light (green) and fluorescence (red) emitted by the rhodamine that diffuses into PDMS. The refractive index change of the solution caused by the rhodamine was negligible due to the low dye concentration. In Fig. 3A, the fluid injection was halted after the channel was filled with both fluorescently doped fluids. In this case, the refractive index in the L-GRIN lens was homogenous due to the complete mixing of the two fluids, and light travelled through the lens without any significant distortion, resulting in a cone-shaped divergent output light path.

To characterize the change of focal length during the variable light focusing process, the L-GRIN lens was subsequently tested at each of the flow conditions used in the ray-tracing simulation (Fig. 2D). Figs. 3B to 3F depict the focusing pattern in the L-GRIN lens at different flow conditions. The trajectories of light were shown to bend smoothly in the fluid-based refractive index gradient and brought into a focal point. The change of the focusing position was evident from the experiments. The images also record the change of the flow patterns within the micro-fluidic channel, which is more evident in the video taken in the same variable focusing process (Video S1 in the ESI†). The experimental results (Figs. 3B to 3F) match well with the ray-tracing simulation (Fig. 2D). The numerical aperture (NA) of the L-GRIN lens varied from nearly zero in Fig. 3B to approximately 0.30 in Fig. 3F ($NA = n\sin\Theta$, where $n = \sim 1.40$ and Θ is half of the output light exit angle after focusing and was measured to be ~0° from Fig. 3B and ~12.5° from Fig. 3F). Such NA is sufficient for on-chip applications such as multi-fiber optical trapping (typical NA ~ 0.1).[5,6] Further optimization of numerical aperture is needed to achieve NA > 1.0, which is necessary for single-fiber optical trap.[7]

The focal distance, defined as the distance between the focusing position and the aperture of the optical fiber, was measured from the simulation and experimental results in Figs. 2 and 3, and plotted as a function of sheath flow rate (Fig. S3 in the ESI†). A good agreement between the simulation and experiment

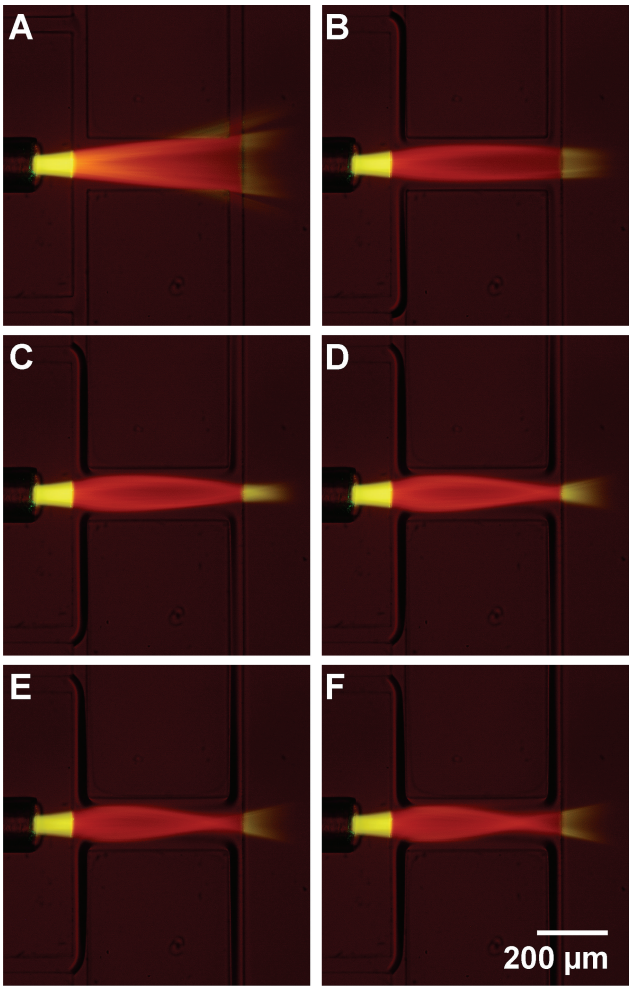

Fig. 3 Ray-tracing experiments for the translation mode to characterize the variable focal length at different flow conditions. (A) Ray tracing for stagnant flow (homogenous refractive index). (B–F) Ray tracing for dynamic flow. The $CaCl_2$ flow rates were fixed at 3.0 μl m^{-1} and the H_2O flow rates were (B) 0.6, (C) 1.2, (D) 1.8, (E) 2.4, and (F) 3.0 μl m^{-1}, respectively.

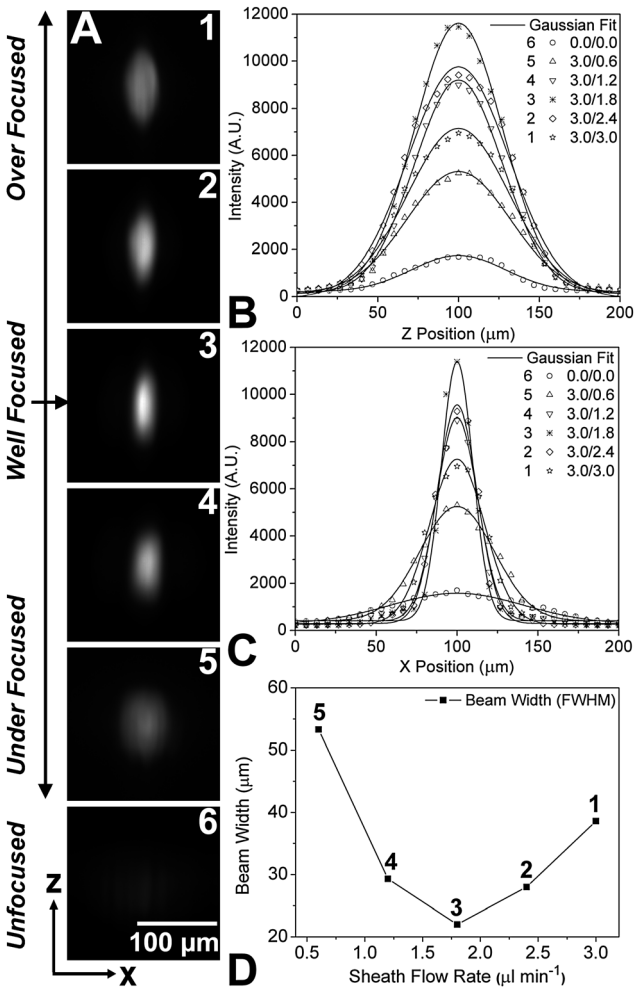

Fig. 4 Characterization of the focused light beam profile in the translation mode. (A) Cross-sectional image of the focused light for different flow conditions (A1: 3.0/3.0, which represents $CaCl_2$ flow rates = 3.0 μl m^{-1} and H_2O flow rates = 3.0 μl m^{-1}; A2: 3.0/2.4; A3: 3.0/1.8; A4: 3.0/1.2; A5: 3.0/0.6; and A6: 0.0/0.0). (B) and (C) are the intensity distributions of the focused light in Z and X directions. The intensity readings were sampled at a 10 μm interval from the images in (A) and fitted with Gaussian curves. The flow conditions are indicated in the graphs (*e.g.*, 3.0/3.0 represents $CaCl_2$ flow rates = 3.0 μl m^{-1} and H_2O flow rates = 3.0 μl m^{-1}). (D) Plot of beam width (FWHM) measured from (C) as a function of sheath flow rate.

was found. The tuning range for the focal distance is approximately from 1,200 to 500 μm as the sheath flow rate increases. It is possible to achieve shorter focal distance, and hence larger NA, by increasing the refractive index contrast (*e.g.*, increasing the concentration of $CaCl_2$ solution or adapting other fluids with higher refractive index).

The optical performance of the L-GRIN lens was further characterized by evaluating the tunability of the beam profile and light intensity. To measure the width and intensity distribution of focused beams, the cross-sectional images of the focused light beams at each flow condition were obtained using a side-view imaging[21,35–37] method (Fig. S2 in the ESI†). The experiment was conducted in a short-version L-GRIN lens (main channel length = 250 μm). A halogen white light source, instead of a laser diode, was used in the experiments due to the better image quality. Measurements were started by setting the $CaCl_2$ solution flow rates at 3.0 μl min^{-1} and H_2O flow rates at 1.8 μl min^{-1}. The sharpest possible cross-sectional image (Fig. 4A3) of the light spot at this flow rate was first obtained, after which the focal plane of the microscope lens and the flow rate of $CaCl_2$ solution were fixed while the H_2O flow rates were adjusted to tune the focusing position. Changes in the shapes and intensities of the light spots demonstrate the focusing effect and tuning behavior. Increasing the H_2O flow rate shortened the focusing distance and causes the light to focus before reaching the microscope focal plane (over-focused, Fig. 4A1 and Fig. 4A2). On the other hand, decreasing the H_2O flow rate caused an increase of the focal distance and under-focused light spots (Fig. 4A4 and Fig. 4A5). In both cases, the focusing positions were moved away from the fixed microscope focal plane, the width of light spots in the X direction increased, and the light intensity decreased. Ceasing the injection of both fluids created an unfocused light spot (Fig. 4A6) of which the intensity was much lower than the sharply focused light spot in Fig. 4A3.

Fig. 4B and 4C show the quantitative analysis of the light intensity distribution along the center lines of focused light spot in X and Z directions. The results indicate that the intensity distributions of focused light beam in both X and Z directions follow the Gaussian distribution. The L-GRIN lens focuses light in the X-Y device plane. Therefore, in the Z direction the peak intensity varied with the flow rate, while the base peak width was maintained at ~160 μm, which is consistent with the width of the divergent beam in the Z direction. In the X direction, however, both the peak intensity and beam width varied with the flow rate. This phenomenon was due to the focusing effect in the X–Y plane. The peak intensity enhancement factor (light intensity in Fig. 4A3 divided by that in Fig. 4A6) was calculated to be ~8, which is among the highest enhancement factors reported.[25]

The full width at half maximum (FWHM) of the beam along the X direction was extracted from the Fig. 4C and plotted as a function of sheath flow rate in Fig. 4D. The minimum width (the well-focused light beam, Fig. 4A3) was estimated to be ~22 μm, which is sufficient for on-chip optical applications such as flow cytometry. We believe that the major limiting factor for further reducing the beam width at the current stage is the aberration of the lens (non-ideal refractive index distribution). In order to achieve higher beam quality, further optimization of the diffusion profile is necessary. This is possible by using more sophisticated and precise methods to control microfluidic diffusion.[38–41]

In order to demonstrate its compatibility with other microfluidic components and potential in lab-on-a-chip applications, we incorporated the L-GRIN lens into a simplified microfluidic flow cytometry device (Fig. 5). The device includes a short-version L-GRIN lens and a neighboring channel with flowing particles (Bangs Laboratories, 9.85 μm polystyrene fluorescent particles, excitation wavelength = 525 nm, emission wavelength = 565 nm). The flow rate of $CaCl_2$ solution and H_2O in the GRIN lens were set at 3.0 μl m^{-1} and 1.8 μl m^{-1}, respectively. These parameters, along with the device geometry, were chosen to ensure that light was focused within the particle channel. Fig. 5A to 5C show three consecutive images of a chain of individual particles travelling through the illumination region defined by the L-GRIN lens. The results show that the fluorescent particle emitted fluorescence (Fig. 5B) only when they entered the illumination region, whereas no fluorescence was observed (Figs. 5A and 5C) from nearby particles outside the illumination area.

Swing mode

The swing mode operates in a slightly different flow condition from the translation mode. The $CaCl_2$ flow rate was kept constant at 3.0 μl m^{-1} from each side (6.0 μl m^{-1} in total from both sides). On the other hand, the H_2O flow rate from each side was adjusted asymmetrically, while keeping the total H_2O flow rate from the two sides constant (6.0 μl m^{-1}). We tested several typical combinations of H_2O flow rates including 5.4/0.6 (abbreviation for 5.4 μl m^{-1} from the left side and 0.6 μl m^{-1} from the right), 4.2/1.8, 3.0/3.0, 1.8/4.2, and 0.6/5.4 μl m^{-1}. The experiments were conducted using a short-version L-GRIN lens in order to achieve a larger swing range.

The CFD simulated $CaCl_2$ concentration distribution for a representative flow condition in the swing mode ($CaCl_2$ flow rate = 3.0 μl m^{-1} on both side, H_2O flow rate = 1.8/4.2 μl m^{-1}) was shown in Fig. 6A. The asymmetrical distribution of the $CaCl_2$ concentration was clearly shown in the simulation. Fig. 6B shows the cross-sectional refractive index profiles at five different locations (cross-sections 1–5, as indicated in Fig. 6A). The results indicate that the $CaCl_2$ concentration (or refractive index) profile was stable along the length of the L-GRIN lens (cross-sections 2–4), which was similar to the observations in the translation mode (Fig. 2B). The profiles at the two ends were not as uniform as those in the translation mode, but they still provide decent refractive index match to PDMS (n = 1.41). Fig. 6C shows the changes of refraction index distribution in the middle of the L-GRIN lens (cross-section 3) with different flow conditions ($CaCl_2$ flow rates = 3.0 μl m^{-1} on both sides, and H_2O flow rates = 3.0/3.0, 1.8/4.2, and 0.6/5.4 μl m^{-1}, respectively). We noted that all refractive index profiles can be well fitted with the HS profiles, expect for a small portion near the edge of the L-GRIN lens (H_2O flow rate = 0.6/5.4 μl m^{-1}). However, this deviation would not affect the focusing result since light was not expected to travel through this portion. We further noted that although the refractive index distributions were no longer symmetric about the centerline of the main channel, they are symmetric about their own axes. The shift of the axis position (indicated by the arrows in the diagram) is evident.

The ray-tracing simulation for the swing mode was conducted using the same method as previously described in the translation mode. The simulated results (Fig. 6D) reveal that in the swing mode the off-optical-axis input light can still be focused toward the optical axis, which leads the output light toward a different

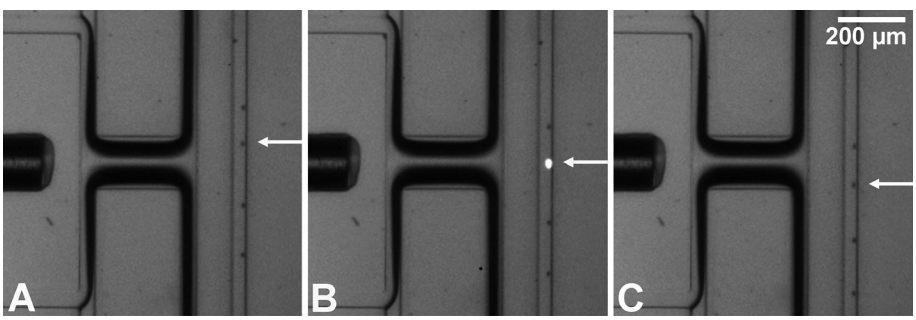

Fig. 5 Consecutive images (A–C) showing the L-GRIN lens integrated with a microfluidic flow cytometry device. The traced particle (highlighted by a white arrow) only emitted fluorescence when entering the light-focusing region near the centre axis of the L-GRIN lens. No fluorescent emission was observed from the neighboring particles that were outside the light-focusing region.

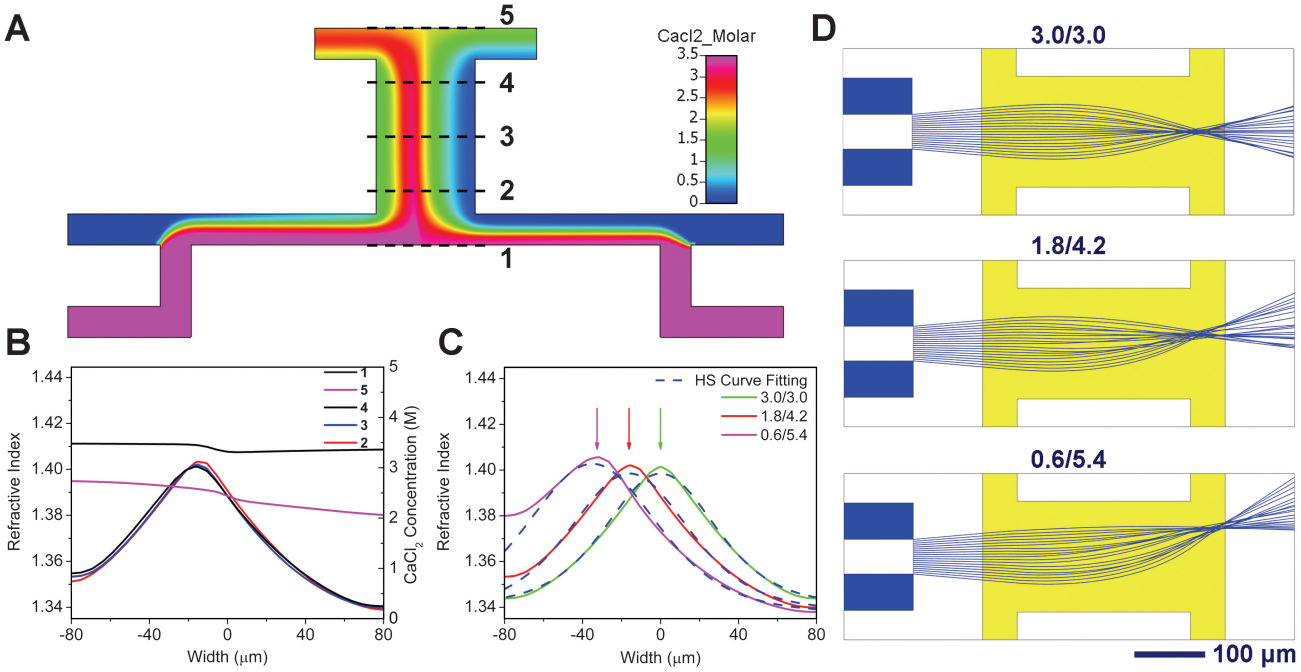

Fig. 6 CFD and ray-tracing simulation for the swing mode. (A) Simulated $CaCl_2$ concentration distribution ($CaCl_2$ flow rates = 3.0 μl m^{-1} on each side, and the H_2O flow rate on the left = 1.8 μl m^{-1}, and the H_2O flow rate on the right = 4.2 μl m^{-1}, abbreviated as 1.8/4.2 μl m^{-1}) in a short-version L-GRIN lens. The color bar represents the molar concentration of $CaCl_2$. (B) Cross-sectional $CaCl_2$ concentration/refractive index profiles at different locations (top to bottom: cross-sections 1, 5, 4, 3, and 2 defined in A). (C) Refractive index profile at the middle of the L-GRIN lens (cross-section 3) for different flow conditions (left to right: $CaCl_2$ solution flow rates were fixed at 3.0 μl m^{-1} on both sides, and the H_2O flow rates were 0.6/5.4, 1.8/4.2, and 3.0/3.0 μl m^{-1}, respectively). Dotted lines are HS curve fitting. (D) Ray-tracing simulation in a short-version L-GRIN lens using the parameters obtained from the CFD simulation. The flow conditions are indicated in the graph (*i.e.*, 1.8/4.2 represents H_2O flow rate = 1.8 μl m^{-1} on the left and 4.2 μl m^{-1} on the right).

direction. They also reveal that the swing angle of the output light can be further adjusted by shifting the position of optical axis. The swing angle increased when H_2O flow rates from each side became further unbalanced. Swing in the opposite side can be conveniently achieved by simply switching the H_2O flow rates.

To experimentally observe the change of the output light propagation in the swing mode, similar ray tracing experiments were conducted as previously described in the translation mode. Both $CaCl_2$ solution and H_2O were dyed with rhodamine to show the light path of focused beam. A short-version L-GRIN lens was operated at the same flow conditions as those used in the simulation (Fig. 6D). Fig. 7 depicts the light focusing patterns at different flow conditions (from 7A to 7E, $CaCl_2$ flow rate = 3.0/3.0 μl m^{-1}, and H_2O flow rates = 5.4/0.6, 4.2/1.8, 3.0/3.0, 1.8/4.2, and 0.6/5.4 μl m^{-1}, respectively). Fig. 7C shows the neutral position of the focused light when the H_2O flow rates on both sides were equal (3.0/3.0 μl m^{-1}). In this case, the refractive index in the L-GRIN lens was symmetric, and light was focused at the centerline of the device. From Fig. 7C to Fig. 7A (or from Fig. 7C to Fig. 7E), the focused output light gradually moved away from the channel centerline as the H_2O flow rates on two sides become increasingly unbalanced. Both the focusing of light and the change of the output light direction were evident. The images also show the change of the flow patterns within the microfluidic channel, which is more evident from a video of the same variable focusing process (Video S2 in the ESI†). The swing angle for each flow rate was measured from the simulation and experimental results in Fig. 6 and Fig. 7 and plotted as a function of the sheath flow rate (Fig. S4 in the ESI†). A good agreement between the simulation and experiment was found. The results show a maximum swing angle of approximately ±12°. A larger swing angle is possible by further optimizing the refractive index gradient and channel geometries.

To the best of our knowledge, the swing mode of in-plane tunable microlenses has never been previously demonstrated. We believe that this additional degree of freedom in tunable microlenses can be of great interest for optics-based lab-on-a-chip applications such as on-chip confocal microscope[42] and trapping/transporting microparticles/cells with fiber-based optical tweezers,[5–7] in which the scanning of the sample or change of the light propagation direction is needed.

Conclusions

In this study, an on-chip tunable optofluidic microlens configuration named L-GRIN lens was presented. In the L-GRIN lens, light is focused due to the gradient refractive index within the liquid medium, rather than curved refractive interfaces used in existing microlenses. This unique microlens mechanism not only enables the flexible changing of the focal distance (translation mode), but also allows shifting of the output light direction (swing mode), a second degree of freedom that to our knowledge has yet to be accomplished for in-plane tunable microlenses. The combination of CFD and ray-tracing simulations proves to be an effective method to numerically prototype the L-GRIN lens. The L-GRIN lens can be readily fabricated *via* the standard

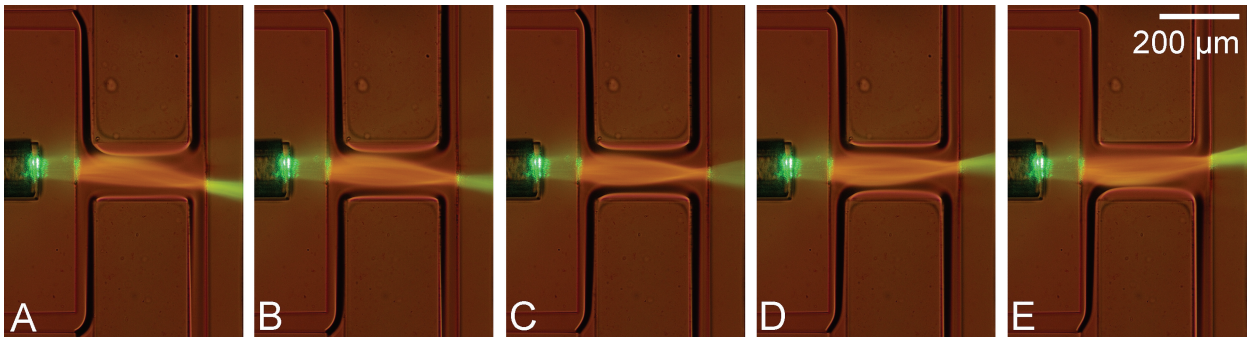

Fig. 7 Ray-tracing experiments for the swing mode to characterize the variable output light direction at different flow conditions. The $CaCl_2$ flow rates were fixed at 3.0 μl m^{-1} on both sides, and the H_2O flow rates were (A) 5.4 μl m^{-1} on the left and 0.6 μl m^{-1} on the right (abbreviated as 5.4/0.6), (B) 4.2/1.8, (C) 3.0/3.0, (D) 1.8/4.2 and (E) 0.6/5.4 μl m^{-1}, respectively.

soft-lithography technique and is highly compatible with other microfluidic components. It also shows a high tunability and strong focusing performance. The NA of the microlens ranges from nearly 0 to 0.3, and the angle of output light direction can be freely adjusted within ±12°. A focused beam width of ~22 μm was achieved, and the peak intensity enhancement factor in the L-GRIN lens was ~8, which is among the highest enhancement factors that have been reported.[25] The operational flow rate of the L-GRIN lens is on the order of a few μl m^{-1}, which is >100 times lower than those in the previously reported in-plane tunable liquid–liquid lenses.[21,25] Such a significant reduction in liquid consumption leads to sustainable operation of the lens and much less stringent requirements in the future on-chip pumping systems for lens control. In summary, the L-GRIN lens delivers excellent flexibility, performance, and compatibility, and it should benefit a wide variety of optics-based lab-on-a-chip applications.

Acknowledgements

We thank Yuebing Zheng, Thomas R. Walker, and Daniel Ahmed for assistance in experiments and helpful discussions. This research was supported by National Science Foundation (ECCS-0824183 and ECCS-0801922) and the Penn State Center for Nanoscale Science (MRSEC). Components of this work were conducted at the Penn State node of the NSF-funded National Nanotechnology Infrastructure Network (NNIN).

References

1 D. Erickson, C. Yang and D. Psaltis, *Photonics Spectra*, 2008, **42**, 74–79.
2 J. Godin, V. Lien and Y. H. Lo, *Appl. Phys. Lett.*, 2006, **89**, 061106/061101–061106/061103.
3 Z. Wang, J. El-Ali, M. Engelund, T. Gotsaed, I. R. Perch-Nielsen, K. B. Mogensen, D. Snakenborg, J. P. Kutter and A. Wolff, *Lab Chip*, 2004, **4**, 372–377.
4 D. Yin, E. J. Lunt, M. I. Rudenko, D. W. Deamer, A. R. Hawkins and H. Schmidt, *Lab Chip*, 2007, **7**, 1171–1175.
5 J. T. Blakely, R. Gordon and D. Sinton, *Lab Chip*, 2008, **8**, 1350–1356.
6 J. Guck, S. Schinkinger, B. Lincoln, F. Wottawah, S. Ebert, M. Romeyke, D. Lenz, H. M. Erickson, R. Ananthakrishnan, D. Mitchell, J. Kas, S. Ulvick and C. Bilby, *Biophys. J.*, 2005, **88**, 3689–3698.
7 C. Liberale, P. Minzioni, F. Bragheri, F. De Angelis, E. Di Fabrizio and I. Cristiani, *Nat. Photon.*, 2007, **1**, 723–727.
8 S. Kuiper and B. H. W. Hendriks, *Appl. Phys. Lett.*, 2004, **85**, 1128–1130.
9 L. Dong, A. K. Agarwal, D. J. Beebe and H. Jiang, *Nature*, 2006, **442**, 551–554.
10 N. Chronis, G. Liu, K. H. Jeong and L. Lee, *Opt. Express*, 2003, **11**, 2370–2378.
11 L. Pang, U. Levy, K. Campbell, A. Groisman and Y. Fainman, *Opt. Express*, 2005, **13**, 9003–9013.
12 Z. Li, Z. Zhang, A. Scherer and D. Psaltis, *Opt. Express*, 2006, **14**, 10494–10499.
13 S. Balslev, A. M. Jorgensen, B. Bilenberg, K. B. Mogensen, D. Snakenborg, O. Geschke, J. P. Kutter and A. Kristensen, *Lab Chip*, 2006, **6**, 213–217.
14 D. V. Vezenov, B. T. Mayers, R. S. Conroy, G. M. Witesides, P. T. Snee, Y. Chan, D. G. Nocera and M. G. Bawendi, *J. Am. Chem. Soc.*, 2005, **127**, 8952–8953.
15 D. B. Wolfe, R. S. Conroy, P. Garstecki, B. T. Mayers, M. A. Fischbach, K. E. Paul, M. Prentiss and G. M. Whitesides, *Proc. Natl. Acad. Sci. USA*, 2004, **101**, 12434–12438.
16 C. L. Bliss, J. N. McMullin and C. J. Backhouse, *Lab Chip*, 2007, **7**, 1280–1287.
17 S. Camou, H. Fujita and T. Fujii, *Lab Chip*, 2003, **3**, 40–45.
18 J. Seo and L. P. Lee, *Sens. Actuators, B*, 2004, **B99**, 615–622.
19 D. Psaltis, S. R. Quake and C. Yang, *Nature*, 2006, **442**, 381–386.
20 C. Monat, P. Domachuk and B. J. Eggleton, *Nat. Photon.*, 2007, **1**, 106–114.
21 X. Mao, J. R. Waldeisen, B. K. Juluri and T. J. Huang, *Lab Chip*, 2007, **7**, 1303–1308.
22 D. Di Carlo, D. Irimia, R. G. Tompkins and M. Toner, *Proc. Natl. Acad. Sci. USA*, 2007, **104**, 18892–18897.
23 A. P. Sudarsan and V. M. Ugaz, *Proc. Natl. Acad. Sci. USA*, 2006, **103**, 7228–7233.
24 Y. Yamaguchi, F. Takagi, K. Yamashita, H. Nakamura, H. Maeda, K. Sotowa, K. Kusakabe, Y. Yamasaki and S. Morooka, *AIChE J.*, 2004, **50**, 1530–1535.
25 S. K. Y. Tang, C. A. Stan and G. M. Whitesides, *Lab Chip*, 2008, **8**, 395–401.
26 M. A. Unger, H. P. Chou, T. Thorsen, A. Scherer and S. R. Quake, *Science*, 2000, **288**, 113–116.
27 M. Zickar, W. Noell, C. Marxer and N. de Rooij, *Opt. Express*, 2006, **14**, 4237–4249.
28 C. Gomez-Reino, M. V. Perez and C. Bao, in *Gradient-Index Optics: Fundamentals and Applications*, eds. C. Gomez-Reino, M. V. Perez and C. Bao, Springer, Heidelberg, 2002, pp. 127–131.
29 D. B. Wolfe, D. V. Vezenov, B. T. Mayers, G. M. Whitesides, R. S. Conroy and M. G. Prentiss, *Appl. Phys. Lett.*, 2005, **87**, 181105.
30 S. K. Y. Tang, B. T. Mayers, D. V. Vezenov and G. M. Whitesides, *Appl. Phys. Lett.*, 2006, **88**, 061112.
31 B. K. Juluri, S.-C. S. Lin, T. R. Walker, L. Jensen and T. J. Huang, *Opt. Express*, 2009, **15**, 2997–3006.
32 C. Gomez-reino, M. V. Perez, C. Bao, M. T. Flores-arias and S. Vidal, *J. Mod. Opt.*, 2000, **47**, 91–102.

33 S.-C. S. Lin, T. J. Huang, J.-H. Sun and T.-T. Wu, *Phys. Rev. B: Condens. Matter*, 2009, **79**, 094302.
34 D. S. Wilkinson, in *Mass Transport in Solids and Fluids*, Cambridge University Press, 2000, pp. 60–65.
35 J. Cao, B. Donell, D. R. Deaver, M. B. Lawrence and C. Dong, *Microvas. Res.*, 1998, **55**, 124–137.
36 J. Leyton-Mange, S. Yang, M. H. Hoskins, R. F. Kunz, J. D. Zahn and C. Dong, *J. Biomed. Eng.*, 2006, **128**, 271–278.
37 X. Mao, J. R. Waldeisen and T. J. Huang, *Lab Chip*, 2007, **7**, 1260–1262.
38 D. Irimia, D. A. Geba and M. Toner, *Anal. Chem.*, 2006, **78**, 3472–3477.
39 N. L. Jeon, S. K. W. Dertinger, D. T. Chiu, I. S. Choi, A. D. Stroock and G. M. Whitesides, *Langmuir*, 2000, **16**, 8311–8316.
40 F. Lin, W. Saadi, S. W. Rhee, S. J. Wang, S. Mittal and N. L. Jeon, *Lab Chip*, 2004, **4**, 164–167.
41 Y. Du, J. Shim, M. Vidula, M. J. Hancock, E. Lo, B. G. Chung, J. T. Borenstein, M. Khabiry, D. M. Cropek and A. Khademhosseini, *Lab Chip*, 2009, **9**, 761–767.
42 S. Kwon and L. P. Lee, *Opt. Lett.*, 2004, **29**, 706–708.